International Journal of Mining Science and Technology 31 (2021) 927–937

Contents lists available at ScienceDirect

International Journal of Mining Science and Technology

journal homepage: www.elsevier.com/locate/ijmst

Dynamic Mode Ⅱ fracture behavior of rocks under hydrostatic pressure using the short core in compression (SCC) method

Wei Yao [a,b,c], Ying Xu [a], Chonglang Wang [d], Kaiwen Xia [a,d,*], Mikko Hokka [c]

[a] State Key Laboratory of Hydraulic Engineering Simulation and Safety, School of Civil Engineering, Tianjin University, Tianjin 300072, China
[b] State Key Laboratory of Explosion Science and Technology, Beijing Institute of Technology, Beijing 100081, China
[c] Engineering Materials Science, Faculty of Engineering and Natural Sciences, Tampere University (TAU), POB 589, FI-33014 Tampere, Finland
[d] Department of Civil & Mineral Engineering, University of Toronto, Toronto, ON M5S 1A4, Canada

ARTICLE INFO

Article history:
Received 31 January 2021
Received in revised form 26 April 2021
Accepted 4 August 2021
Available online 17 August 2021

Keywords:
Loading rate
Finite element method
Mode Ⅱ fracture toughness
Fangshan marble
Hydrostatic pressure
Short core in compression

ABSTRACT

The shear failure of rocks under both a static triaxial stress and a dynamic disturbance is common in deep underground engineering and it is therefore essential for the design of underground engineering to quantitatively estimate the dynamic Mode Ⅱ fracture toughness K_{IIC} of rocks under a triaxial stress state. However, the method for determining the dynamic K_{IIC} of rocks under a triaxial stress has not been developed yet. With an optimal sample preparation, the short core in compression (SCC) method was designed and verified in this study to measure the dynamic K_{IIC} of Fangshan marble (FM) subjected to different hydrostatic pressures through a triaxial dynamic testing system. The formula for calculating the dynamic K_{IIC} of the rock SCC specimen under hydrostatic pressures was obtained by using the finite element method in combination with secondary cracks. The experimental results indicate that the failure mode of the rock SCC specimen under a hydrostatic pressure is the shear fracture and the K_{IIC} of FM increases as the loading rate. In addition, at a given loading rate the dynamic rock K_{IIC} is barely affected by hydrostatic pressures. Another important observation is that the dynamic fracture energy of FM enhances with loading rates and hydrostatic pressures.

1. Introduction

In deep underground space excavations and deep rock engineering practices, rocks are generally subjected to a high in-situ stress (i.e. a static triaxial stress state or a hydrostatic pressure) [1,2], and these natural rocks are also likely to fracture failure induced by dynamic forces, e.g. optional blasting and earthquake. Therefore, it is crucial to quantify the dynamic fracture properties of deep rocks under both the dynamic load and the in-situ stress [3–8].

The fracture toughness of rocks is one of the crucial fracture properties of rocks and many investigations have been performed to assess the rock fracture toughness under different loading conditions [9–12]. There are three primary fracture modes (i.e. Modes Ⅰ, Ⅱ, and III) for the determination of rock fracture toughness [13]. A amount of experimental specimens have been proposed to obtain different types of the fracture toughness of rock-like materials under static loading conditions: (1) Mode Ⅰ (opening): cracked chevron notched Brazilian disc [14–17], short rod/beam [18–20], chevron bending [18], and notched semi-circular bend (NSCB) method [10,21]; (2) Mode Ⅱ (shearing): antisymmetric four-point bending specimen [22–29], punch-through shear (PTS) specimen [30–32], and short core in compression (SCC) specimen [33]; and (3) mixed mode Ⅰ/Ⅱ: Arcan specimen with a notch for uniform plane stress [34–36], the NSCB with inclined notch [37–39], and cracked straight-through Brazilian disc specimen [14]. Among the methods mentioned above, the International Society for Rock Mechanics and Rock Engineering (ISRM) has suggested the NSCB method to quantify the dynamic Mode Ⅰ fracture toughness K_{IC} of rocks [40].

Generally, the main fracture mode for engineering materials (e.g. alloys and concretes) is Mode I fracture. However, in natural rock structures, Mode Ⅱ or mixed mode Ⅰ/Ⅱ failure frequently happen due to the complex mutual effect between tensile and shear fracture [9,41,42]. For example, discontinuities in rock masses and rocks with pre-existing cracks are commonly failures as a shear mode when they are subjected to compressive/shear mixed mode forces [5,43]. Hence, shearing failure is the normal mode in

* Corresponding author.
E-mail address: kaiwen.xia@utoronto.ca (K. Xia).

https://doi.org/10.1016/j.ijmst.2021.08.001
2095-2686/

rock engineering and it is essential to study the Mode Ⅱ fracture toughness K_{IIC} of rocks [33,44,45].

Several researchers have studied the K_{IIC} of materials under static loading conditions [39,43,46–48]. Watkins and Liu [46] introduced a short beam in compression (SBC) specimen to quantify the K_{IIC} of plain concrete due to the simple specimen and loading configuration of the SBC method. Lawn [49] claimed that the shearing fracture toughness probably depends on the normal pressure on the plane of failure. Melin [50] pointed out that under high confining pressures the Mode Ⅱ fracture is dominated in the rock failure. Whittaker et al. [51] gave a review of various approaches for measuring the K_{IIC}. Rao et al. [43] measured the pure K_{IIC} in the mixed mode loading and found the K_{IIC} for the same rock is higher than the K_{IC}. Backers et al. [31] and Backers et al. [30] examined the effect of the confining pressure on the K_{IIC} by means of the PTS method with confining pressure. Lee [52] employed the rectangular PTS specimens to measure the K_{IIC} of rocks. Due to the advantages of a core-based specimen with confinement, the PTS method has been accepted in 2012 by the ISRM to quantify the dynamic static K_{IIC} of rocks under different confining pressures [47]. Furthermore, Jung et al. [53] used the SCC method with a cylindrical rock core to replace the short cuboid beam in the compression method and further measured the shear strength and K_{IIC} of rock under static loading based on the SCC method. Xu et al. [33] evaluated the validity of the SCC method for measuring the K_{IIC} and calculated the stress intensity factor (SIF) and the K_{IIC} of the SCC specimen.

The above investigations emphasized on the K_{IIC} of rocks under static loading conditions. However, the methods for quantifying the dynamic K_{IIC} were recently developed. The PTS specimen was recently extended to measure the dynamic rock K_{IIC} [5] and the SCC specimen in combination with a split Hopkinson pressure bar (SHPB) system was suggested to obtain the dynamic rock K_{IIC} [54]. Furthermore, the PTS specimen was modified to determine the dynamic rock K_{IIC} with confining pressures [55].

Although the static and dynamic K_{IIC} of rocks under confining pressures was extensively determined, there is a lack of a method to quantify the dynamic rock K_{IIC} over various in-situ stresses or hydrostatic pressures. Therefore, a dynamic SCC method for determining the K_{IIC} of rocks under a hydrostatic pressure is proposed in this work. Compared with the numerous testing methods for obtaining the dynamic rock K_{IIC}, the SCC method is easily applicable to the dynamic apparatus with the hydrostatic pressure loading system and has an easy preparation with core-based specimen [33]. Also, the Mode Ⅱ fractures initiate along the notch-tips in the SCC method [33]. A triaxial SHPB system is utilized to exert both a hydrostatic pressure and a dynamic force to the SCC specimen. The dimensions of the dynamic SCC specimen with the hydrostatic pressure are redesigned to reach the dynamic stress equilibrium [40,56]. The dynamic fracture mode and fracture energy of the rock SCC specimen over various hydrostatic pressures are discussed.

In this study, the dynamic experimental apparatus for the hydrostatic pressure loading and the SCC specimen preparation are presented, following by the quantification of the K_{IIC} of the SCC specimen under the hydrostatic pressure. After that, the fracture pattern and the dynamic rock K_{IIC} under different hydrostatic pressures are discussed.

2. Experimental methodology

2.1. Specimen preparation

The SCC specimen is generally a cylinder with two parallel half-through notches from opposite sides, as shown in Fig. 1a.

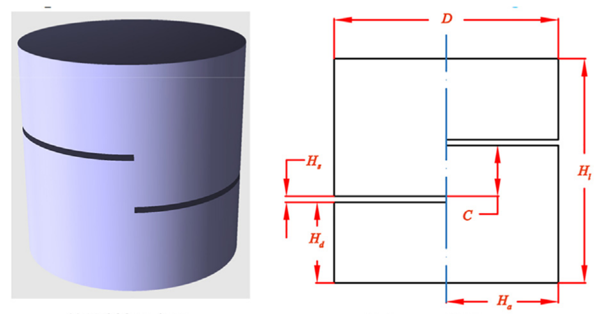

(a) 3D SCC specimen   (b) Geometry of SCC specimen

Fig. 1. SCC specimen (H_l is the length, D is the diameter, $H_a = D/2$ is the notch depth, H_s is the notch thickness, C is the distance between two notches, which are parallel to the specimen ends.).

The distance from the notch to its nearest core end is the same for both upper and low notches and thus defined as H_d in Fig. 1b. In addition, the fronts of these two notches are parallel, creating a rectangular rock bridge in the central plane along the core axis (Fig. 1). Under a uniaxial compression, the shear stress is generated in this rectangular bridge of the SCC specimen. Hence, the Mode Ⅱ fracture is induced in this bridge that can be considered as a fracture plane.

In the previous studies, the SCC specimen with a 38-mm diameter was employed in a static test [33] and the SCC specimen with a 50-mm diameter was used in a dynamic test [53]. Thus, the SCC specimen with a 38-mm diameter is applied in this study because this diameter is compatible with the dynamic loading system.

The existing studies have indicated that the Mode Ⅱ SIF of the SCC specimen is mainly affected by the geometry factor C/D and C/H_l [33,54]. Meanwhile, the dynamic stress equilibrium in the rock sample is a precondition for a valid dynamic rock SHPB test [40]. In such a case, the short rock specimen can easily accomplish the dynamic stress equilibrium. In addition, $H_l/D = 1$ was successfully employed in the previous dynamic SCC test [54]. Therefore, the height of the SCC specimen is chosen as 38 mm in this study to easily reach the dynamic stress equilibrium in the rock specimen.

Because the small variation of SIF is close to the ideal case for the Mode Ⅱ shear failure, the small value of C/H_l is recommended by researchers [33,53,54]. Meanwhile, the studies have indicated that the shear stress depends on the value of C/H_l [33,46,54]; that is, if $C/H_l \geq 0.3$, the SCC specimen is a tensile failure and invalid for measuring the K_{IIC} of rocks [33,46]. Thus, $C/H_l = 0.2$ is selected in this study to generate shear failure in the fracture plane. In addition, to ensure the symmetry of shear stress around two notch-tips in the SCC specimen, two parallel notches have the identical distance H_d to the corresponding end surfaces. Also, the fronts of these two notches are parallel to each other (as shown in Fig. 1). As discussed above, the configuration of the dynamic SCC specimen is summarized in Table 1.

Table 1
Configuration of SCC specimen.

Property	Value
Distance between two notches, C (mm)	7.6
Diameter, D (mm)	38.0
Length, H_l (mm)	38.0
Notch depth, H_a (mm)	19.0
Notch thickness, H_s (mm)	1.0
C/D	0.2
C/H_l	0.2

To manufacture the SCC specimen, rock cylinders with desired diameter and length were machined. Based on the requirements for the dynamic rock specimen in the SHPB test [40], all surfaces of the SCC specimen should be smooth without abrupt irregularities. Henceforth, two half-through notches were made with slow cutting speed to guarantee smooth notch surfaces. The thickness of the notches should be not greater than 1 mm.

In this study, the dynamic SCC specimen is made from fine-grained Fangshan marble (FM). The primary properties of FM are detailed in Table 2 [5,57–59]. The mineral analysis and microscopic observation in the authors' previous studies [5,57] indicated that FM can be considered as a homogeneous and isotropic material, and thus it is suitable for demonstrating the feasibility of the proposed dynamic SCC method with triaxial stresses. The photo of the original SCC specimen made from the FM is shown in Fig. 2.

2.2. Dynamic SCC method with hydrostatic pressure

The dynamic Mode Ⅱ fracture failure experiments with the SCC specimen under the hydrostatic pressure were conducted by using the triaxial dynamic testing system, which was proposed in the authors' earlier study [60]. As shown in Fig. 3, this triaxial dynamic testing system comprises a dynamic loading device and a static triaxial loading apparatus. The dynamic loading system is also a traditional SHPB system (Fig. 3b). This dynamic loading system is undertaken to exert dynamic compressive forces on the SCC specimen. Meanwhile, the static triaxial loading apparatus is utilized to act the hydrostatic pressure on the SCC specimen before dynamic loading. As shown in Fig. 3b, Cylinder 1 produces lateral confinement on the SCC specimen, and Cylinder 2 provides the axial pressure to the SCC specimen. Because the axial pressure and the confinement pressure on the SCC specimen are separately exerted by two cylinders, the dynamic load can be easily applied to the SCC specimen. The hydrostatic pressure on the SCC specimen can be reached when the pressures of these two cylinders are identical. Thus, in this study, both Cylinder 1 and Cylinder 2 are linked to the same oil pressure unit. The SCC specimen is first placed in the dynamic loading system and is then immersed into oil in Cylinder 1. Subsequently, axial forces are acted on the specimen/bar interfaces through the pressure from Cylinder 2 since the rigid frame controls the leftward movement of the incident bar (Fig. 3b) and two tie-rods constrain the relative motion of two cylinders (Fig. 3b). In addition, the lateral pressure on the residual portion of the SCC specimen is acted by the oil pressure σ_1 in Cylinder 1. The combination of the pressures in Cylinder 1 (σ_1) and Cylinder 2 (σ_2) provides the triaxial stress on the whole SCC specimen [60]. Although the hydraulic pressure in Cylinder 1 provides the axial pressure on the notch surfaces, the axial pressures on the notch surfaces are offset due to the symmetry of the notch surfaces. With the force equilibrium on the specimen/bar interfaces, the SCC specimen can be subjected to a hydrostatic pressure if $\sigma_1 = \sigma_2 = \sigma_h$ (where σ_h is the hydrostatic pressure, as shown in Fig. 3b).

Table 2
Basic mechanical and physical properties of manufactured FM specimens.

Property	Value
Density (g/cm^3)	2.85
Young's modulus (GPa)	85
Poisson's ratio	0.3
P-wave velocity (m/s)	5900
Compressive strength (MPa)	155
Tensile strength (MPa)	9.5
K_{IC} (MPa·m$^{1/2}$)	1.5

When the expected level of the hydrostatic pressure is reached on the SCC specimen, the incident stress wave ε_i (which is produced by the striker impact) can efficiently propagate rightward because the rightward dynamic stress wave is barely influenced by the small flange [60,61]. Similar to the traditional SHPB test, the reflected stress wave ε_r and the transmitted stress wave ε_t are generated at the interface between the SCC specimen and the bars. Fig. 4a illustrates the original signals in a typical dynamic SCC test. These three waves were obtained from the strain gauges on bars and recorded by a digital oscilloscope after amplification. In this study, because alternating current (AC) coupling is implemented in an oscilloscope, the dynamic stress strains were merely detected in the Wheatstone bridge circuit. Consequently, one can see from Fig. 4a that the baselines of voltage in the original signals align with zero in the dynamic SCC tests with hydrostatic pressure [4].

According to the rock dynamic testing methods suggested by the ISRM [40], a valid dynamic rock test by using the SHPB system should satisfy the dynamic stress equilibrium on the rock sample before the failure point [56]. Therefore, the pulse shaper (Fig. 3b) was utilized in this study to reach the dynamic stress equilibrium [40]. Here, the dynamic stress equilibrium is expressed as

$$P_1(t) \approx P_2(t) \tag{1}$$

where P_1 is the force on the left loading end of the specimen, $P_1(t) = AE(\varepsilon_i(t) + \varepsilon_r(t))$; P_2 the force on the right loading end of the specimen, $P_2(t) = AE\varepsilon_t(t)$; t the time; and A and E the cross-sectional area and Young's modulus of the bars, respectively. Fig. 4b illustrates these two dynamic forces in a typical SCC test. Before the peak values of these forces are applied to the SCC specimen, the force P_1 is nearly equal to the force P_2. In addition, it has been verified that the peak value of the dynamic force on the SCC specimen is matched with the specimen shear failure if the dynamic stress equilibrium is reached [54]. Therefore, one can see that the dynamic stress equilibrium is reached before the shear failure of the SCC specimen. The dynamic force equilibrium for each dynamic SCC test has been critically evaluated to ensure that the valid dynamic K_{IIC} of rock specimens can be obtained under various hydrostatic pressures.

2.3. Dynamic fracture energy measurement for the SCC method with hydrostatic pressure

The stress wave energy W in the dynamic SCC test is expressed as follows [62].

$$W = \int_0^t E(\varepsilon(\tau))^2 A v_p \mathrm{d}\tau \tag{2}$$

where τ is the time integral variable; v_p the one-dimensional P wave velocity of the bars; and ε the time-resolved strain (i.e. ε_i, ε_r, and ε_t). Since the wave impedance of steel bars is massively different from that of the hydraulic oil, the stress waves in bars are mostly transmitted into the SCC specimen and the authors assume that most of the energy is consumed by the specimen during the dynamic SCC test with the hydrostatic pressure [63]. As a result, the energy consumed during the dynamic SCC test can be quantified; that is, the total energy dissipation in the SCC specimen ΔW equals the energy difference between the incident energy (W_i) and the sum of the reflected energy (W_r) and the transmitted energy (W_t) [64].

$$\Delta W = W_i - (W_r + W_t) \tag{3}$$

The energy dissipation in the SCC specimen is comprised of two components: the creation of new crack surfaces (W_G) and the kinetic energy R in the two parts of the failed SCC specimen. Namely, $R = mv^2/2$, where m is the fragment mass and v is the

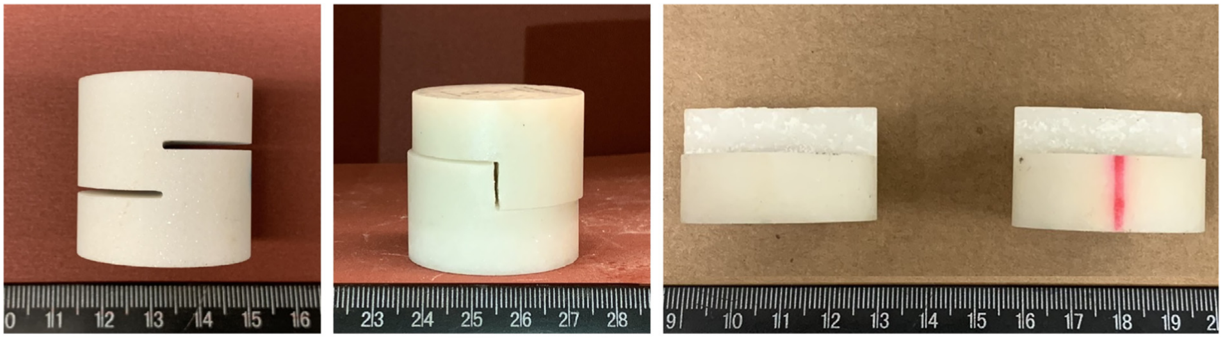

(a) Original SCC specimen (b) Recovered SCC specimen (c) The fracture surfaces of the tested SCC specimen

Fig. 2. A typical SCC specimen before and after the test.

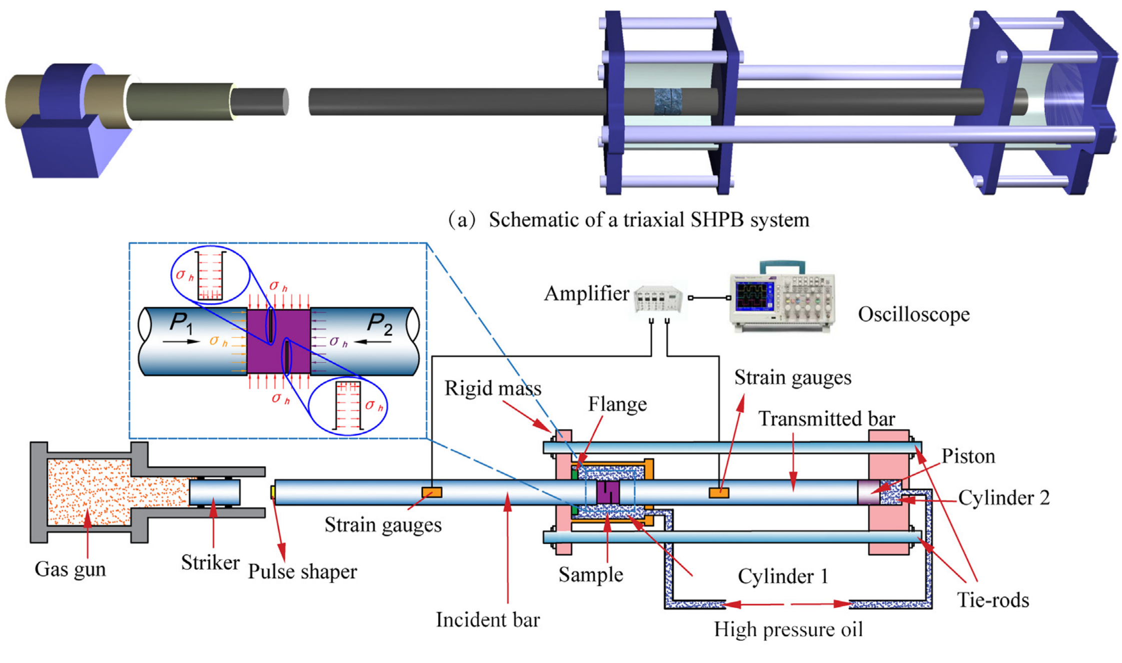

(b) Dynamic loading system, static triaxial loading apparatus and data acquisition system

Fig. 3. Triaxial SHPB testing system.

fragment velocity, which was obtained by using the speed of the bar end because the specimen ends are not detached to the bar ends during the dynamic loading period. The velocities at the incident bar end (v_1) and the transmitted bar end (v_2) are

$$v_1(t) = v_p(\varepsilon_i(t) - \varepsilon_r(t)),\ \ v_1(t) = v_p\varepsilon_t(t) \tag{4}$$

In such a case, the energy for the new crack surface created by the dynamic shear loading can be calculated as

$$\begin{aligned} W_G &= \Delta W - R \\ &= \Delta W - \left(\frac{1}{2}\int_0^t m_1(v_1(\tau))^2 d\tau + \frac{1}{2}\int_0^t m_2(v_2(\tau))^2 d\tau\right) \end{aligned} \tag{5}$$

where m_1 and m_2 are the masses of two fragments, respectively. Thus, the dynamic shear fracture energy of the SCC specimen under hydrostatic pressure can be estimated by the above equation.

3. Determination of the K_{IIC} in SCC specimens under hydrostatic pressure

3.1. Deduction of the Mode II fracture toughness

It has been proven that the K_{IIC} of the SCC specimen under both static and dynamic conditions can be calculated by the peak load on the loading end of the SCC specimen [33,53,54]. Consequently, the formula for determining K_{IIC} (MPa·m$^{1/2}$) of SCC specimens can be generally written as

$$K_{IIC} = \alpha\sigma_{max} \tag{6}$$

where σ_{max} is the peak compressive stress on the SCC specimen (MPa); and α depends on the geometry of the SCC specimen. In addition, according to the ISRM suggested method to obtain the rock K_{IIC} via the PTS specimen under confinement pressure [47], the K_{IIC} of rocks through the SCC specimen under hydrostatic pressure can be similarly estimated as follows.

$$K_{IIC} = \alpha\sigma_{max} + \beta\sigma_h \tag{7}$$

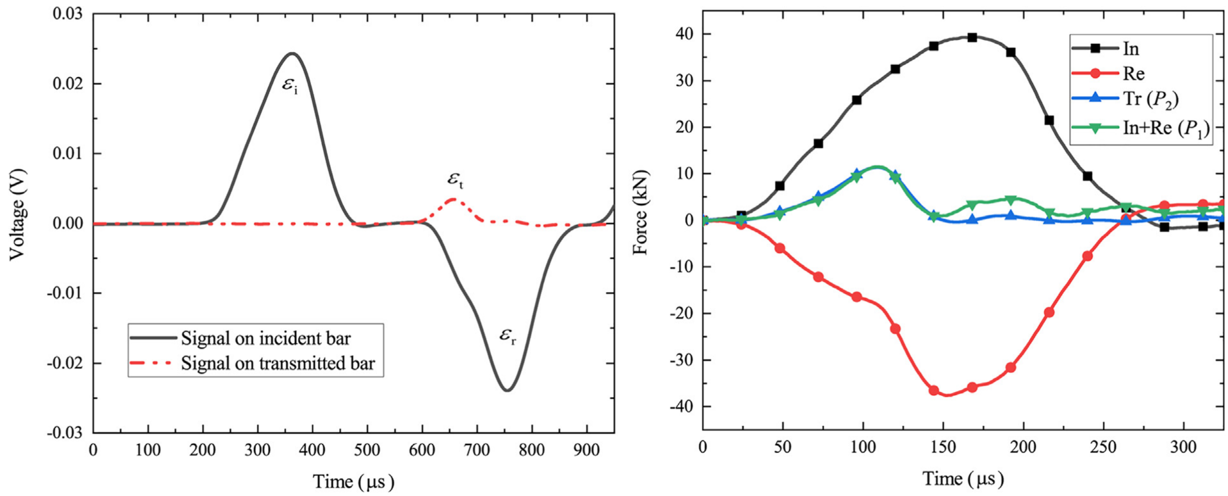

(a) Original strain signals on bars in a typical test (b) Dynamic force equilibrium in a typical dynamic SCC test

Fig. 4. Original strain signals on bars and dynamic force equilibrium in a typical dynamic SCC test with the hydrostatic pressure of 10 MPa (“In”, “Re”, and “Tr” denote “incident”, “reflected”, and “transmitted”, respectively).

where β is the geometry parameter determined by the numerical simulation [33,53,54] in a combination of the *J*-integral method [13,33,65,66] and the displacement extrapolation technique [47,67]. The *J*-integral method is a simple and effective approach with good accuracy and has been prevalently used to estimate the SIF around the crack-tip. Therefore, the finite element analysis (FEA) in a combination of the *J*-integral method is applied to determine the values of two geometry parameters (α and β) and to further calculate the K_{IIC} of the rock SCC specimen under the hydrostatic pressure. In such a case, it is essential to generate a valid finite element model of the SCC specimen and then determine these two parameters with the verified finite element model. The numerical SCC model was constructed to analyze the stress field in the SCC specimen and verify the finite element model for the SIF calculation at the crack tip.

3.2. Stress distribution in SCC specimens

A three-dimensional (3D) finite element model, as shown in Fig. 5, was established via a commercial program ABAQUS to investigate the stress distribution inside the SCC specimen. The SCC specimen geometry for dynamic experiments is used in the 3D model, i.e. C/H_l = 0.2 and H_l/D = 1. This numerical model is comprised of 423152 nodes and 402960 eight-node quadratic plane-strain hexahedral elements with linear geometric order. In this model, the SIF was estimated by using the *J*-integral method, in which the energy release associated with crack growth was characterized around the crack tip. The energy release rate is given by $\bar{J} = \int_A \lambda(s)\mathbf{n}\cdot\mathbf{H}\cdot\mathbf{q}\,dA$, where $\lambda(s)$ is a virtual crack advance, d*A* is a surface element along a vanishing small tubular surface enclosing the crack tip or crack line, **H** is an equation in terms of the elastic strain energy density and the stress vector, **n** is the outward normal to d*A*, and **q** is the local direction of virtual crack extension [67,68]. The energy release can be related to the SIF when the material response is linear. Thus, in this numerical model, only elastic modulus and Poisson’s ratio were set as the corresponding values in Table 2. As shown in Fig. 5a, the compressive loading was acted on both the upper and bottom ends of the SCC specimen.

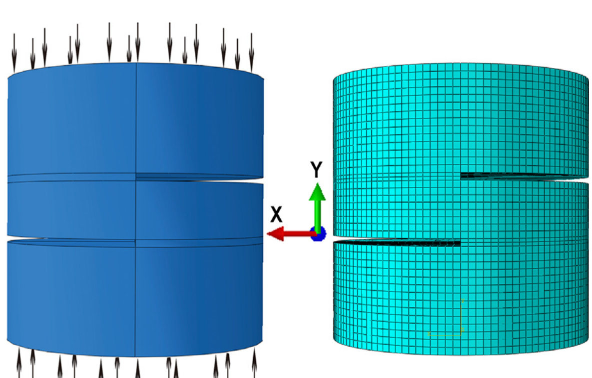

(a) Loads of the 3D SCC model (b) Meshes of the 3D SCC model

Fig. 5. Configuration of the 3D SCC model.

Due to the symmetrical configuration of SCC samples, the XY central plane, which is normal to the failure surface, can represent the shear stress distribution along the failure surface. Thus, based on the shear stress field of the central plane in the 3D specimen in Fig. 6, the peak shear stress is located at the notch-tip, indicating that the shear failure occurs at the notch tips. Also, the hydrostatic pressure applied on the SCC specimen has barely influence on the shear stress. Furthermore, the shear stress on the upper notch-tip of a typical SCC model is given in Fig. 7. One can see that the maximum shear stress is reached at the XY central plane, which can be considered as the critical plane for shear fracture. Consequently, the stress field on the critical plane can characterize the stress state when the shear failure commences in the SCC specimen. The SIF at notch-tips (in the center of which shear fractures occur) is determined based on the stress distribution in the critical plane. In such a case, a 2D model on the critical plane was built to efficiently examine the shear stress distribution and further to determine the SIF at notch-tips where shear fractures initiate.

3.3. Numerical model for the SCC method

According to the geometry of the critical plane of the SCC specimen, the 2D SCC model was created by using 5776 nodes and 5548 eight-node quadratic elements. The elastic modulus and Poisson’s ratio were set as the corresponding values in Table 2. The axial compressive stress was acted on both the upper and bottom ends of the SCC model. Based on the shear stress field on the central plane of the SCC specimen under different hydrostatic

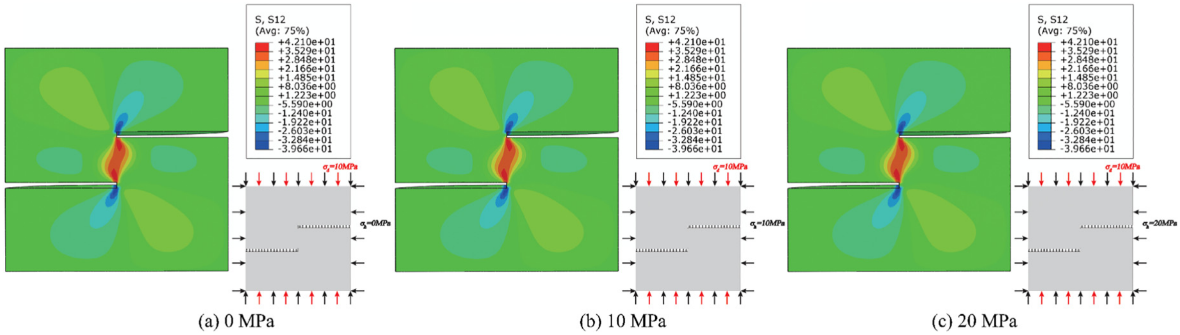

Fig. 6. Shear stress distribution (MPa) on the central plane of the 3D SCC model over the axial compressive stress of 10 MPa with different hydrostatic pressures.

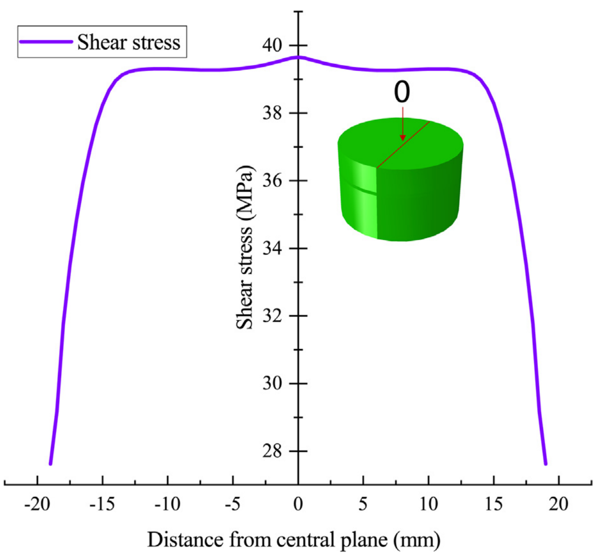

Fig. 7. Shear stress on the upper notch of the 3D SCC sample under the compressive stress of 10 MPa without hydrostatic pressure (the line in the inset illustrates the nodes of the upper notch and 0 is the central plane).

pressures in Fig. 8, the hydrostatic pressure has barely influence on the shear stress in the SCC specimen. A shear zone (red zone in Fig. 8) is formed between these two notch-tips and the maximum shear stresses appear at both two notch-tips. The shear stresses between these two notch-tips are almost constant and a region with a high shear stress is created along the potential shear failure path between these two notch-tips. This shear stress distribution may result in the shear failure that occurs between two notch-tips. Therefore, the SCC geometry in this study is valid for the shear failure under various hydrostatic pressures. In addition, the distributions of the principal stress for different hydrostatic pressures are shown in Fig. 9. For all hydrostatic pressure conditions, the major principal stress (tensile) is distributed along the bridge of these two notch-tips. However, the principal stress in the residual area is uniformly close to zero. The result of the 2D simulation is consistent with that reported by other researchers [33,46,53]. As a result, the 2D numerical analysis here is valid to determine the stress state and the SIF around the notch-tip in the SCC specimen.

The fracture toughness is determined by the critical value of the SIF at the notch-tip. Based on the static and dynamic SCC experiments and the numerical simulation for the SCC specimen [33,53,54], the shear fracture is normal to the notch plane. This differs from the PTS specimen and the shear box test, in which the shear fractures nearly grow along the notch plan. Hence, a secondary crack in the direction of the notch is unnecessary to obtain the SIFs at the notch-tips in simulation analysis if the crack plane is along the notch plane, such as the PTS test and the shear box test. However, based on fracture mechanics theory, the secondary crack is a precondition for accurately determining the SIF in the fracture process [69–71], and the K_{IIC} can be further determined precisely when a crack tip exists along the shear fracture plane [72]. The methodology for using a secondary crack was initially used in the wing crack model [70], in which secondary cracks were originated from the wing crack-tips and the SIF is derived from the limit if the length of the secondary cracks approach zero. This model has been widely used in fracture mechanics analysis because it estimated primely the ultimate strength measured in the experiments and the direction of the general failure plane [70]. Recently, based on this method, Xu et al. [33] introduced secondary cracks at the notch-tips to obtain the SIF of the SCC specimen under static uniaxial compression. Thus, secondary cracks at notch-tips along the shear fracture plane were used in this study to estimate the SIF of the dynamic SCC sample. As shown in Fig. 10a, secondary cracks (l_c) are introduced in the 2D SCC finite element model validated above. These two secondary shear cracks are perpendicular to

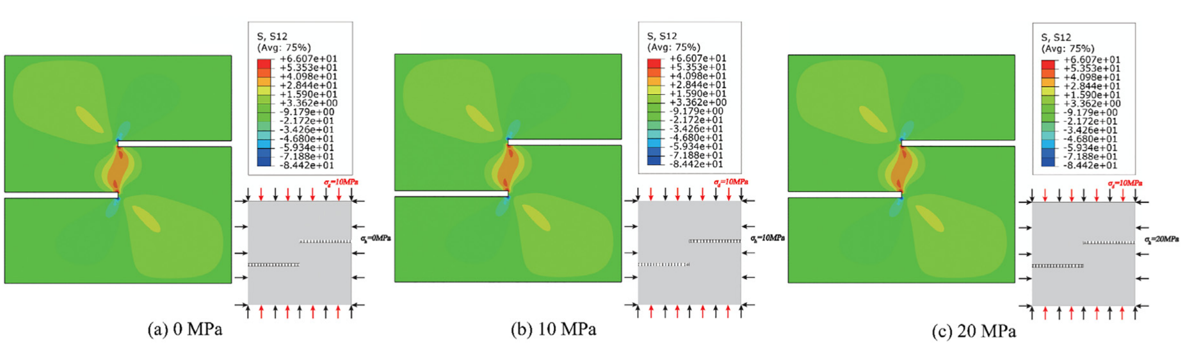

Fig. 8. Shear stress (MPa) distribution of the 2D SCC model under the axial compressive stress of 10 MPa with different hydrostatic pressures.

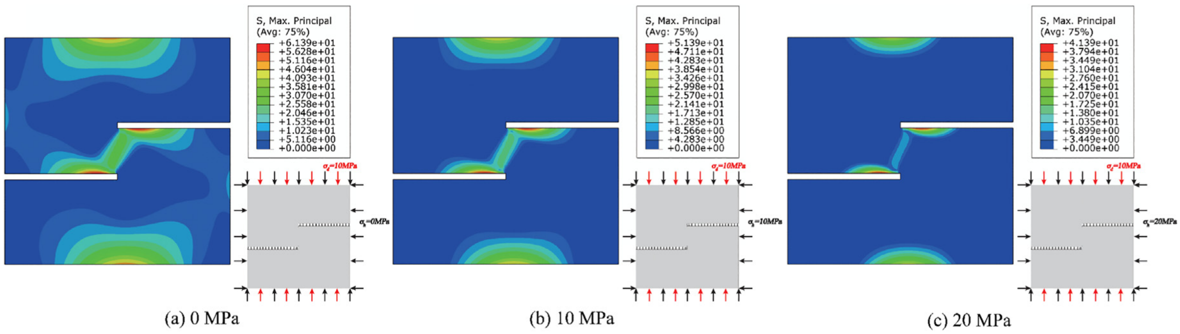

Fig. 9. Principal stress (MPa) distribution of the 2D SCC model under the axial compressive stress of 10 MPa with different hydrostatic pressures.

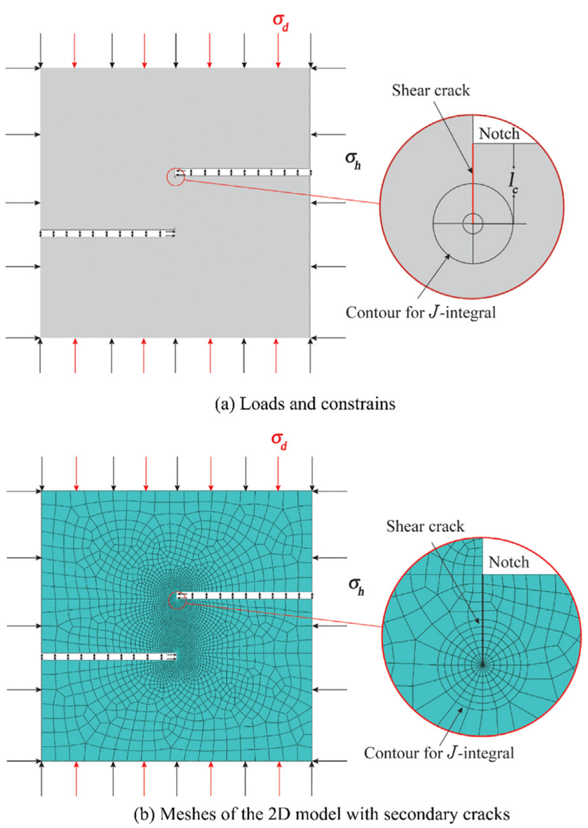

Fig. 10. Loads and meshes of the 2D model under the axial compressive stress (σ_d) and the hydrostatic pressure (σ_h).

the notch-tips. This model was constructed by ABAQUS and the singular quadrilateral eight-node elements were employed to mimic the singularity at secondary crack-tips (Fig. 10b). This model with the secondary cracks includes 5438 elements as illustrated in Fig. 10b. The SCC model was under six hydrostatic pressures (i.e. 0, 5, 10, 15, 20, and 25 MPa) and seven axial compressive loads (i.e. 5, 10, 15, 20, 25, 30, and 35 MPa). The SIFs at the shear crack-tips in the SCC specimen were determined by using the *J*-integral method [13,65,66], which is embedded in the finite element program ABAQUS and has been extensively utilized by many researchers to determine the SIFs due to its reliability [10,33,73,74].

3.4. Determination of Mode Ⅱ SIF of the SCC specimen under hydrostatic pressure

Based on the energy analysis, the Mode Ⅱ SIF at the shear crack-tip (K_{II}^{*}) of the SCC specimen and short beam specimen under static loading condition without hydrostatic pressure can be generally expressed as [33,46]

$$K_{\text{II}}^{*} = Y(C/H_l)\sqrt{\pi H_a}\cdot(P/DC) \tag{8}$$

where $Y(C/H_l)$ is a geometrical function; P the compressive force; and $P/(DC)$ can be considered as a nominal shear stress acting on the shear plane. Hence, the geometrical function Y can be obtained by

$$Y(C/H_l) = \left(K_{\text{II}}^{*}/\sqrt{\pi H_a}\right)/(P/DC) \tag{9}$$

Based on Eq. (9), the K_{II}^{*} of SCC specimens under the specific geometry is obtained via the displacement extrapolation technique in the foregoing finite element model with secondary cracks [75]. In the displacement extrapolation technique, the Mode Ⅱ SIF around the shear crack-tip (K_{II}) is calculated by using the FEA with the *J*-integral method, and then the K_{II}^{*} can be obtained with the extrapolation of the K_{II} around the crack-tip.

The K_{II} is illustrated in Fig. 11 in terms of the length of the shear crack l_c under the axial compressive load of 5 MPa. It demonstrates that K_{II} enhances almost linearly with l_c for all hydrostatic pressure conditions. The hydrostatic pressures have no influence on the values of K_{II}. In addition, the K_{II} is given as a function of l_c under the hydrostatic pressure of 10 MPa in Fig. 12. It can be seen that the K_{II} increases almost linearly with l_c for all axial compressive loading conditions. Thus, the K_{II}^{*} of the SCC specimen is determined by extrapolating K_{II} to $l_c = 0$, and the K_{II}^{*} of SCC specimens under differ-

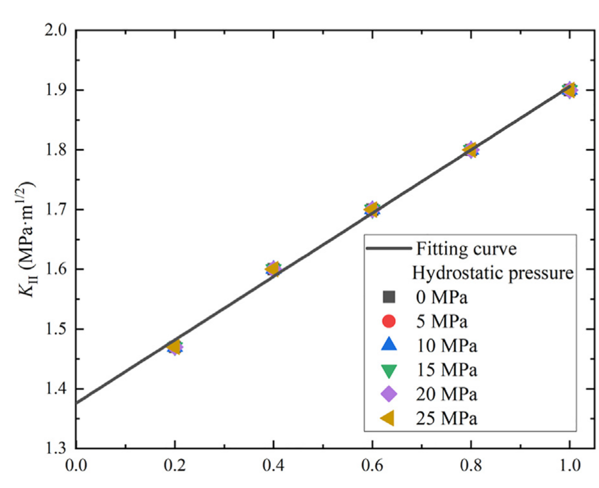

Fig. 11. SIF around crack tip in the SCC specimen under different hydrostatic pressures using the extrapolation method (The axial compressive load is 5 MPa).

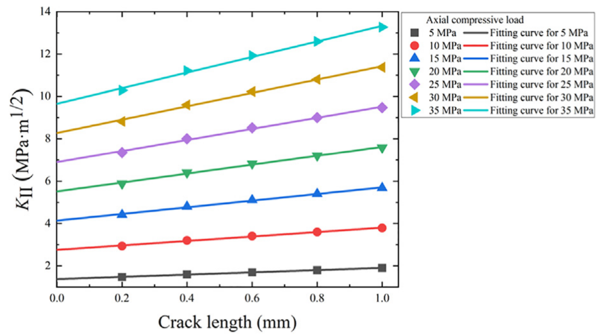

Fig. 12. SIF around crack tip in the SCC specimen under different axial compressive loads using the extrapolation method (The hydrostatic pressure is 10 MPa).

ent compressive loads and hydrostatic pressures can be determined as the intercept for the fitting curves in both Figs. 11 and 12.

According to the method above, the values of K_{II}^* for the SCC specimen under various hydrostatic pressures and different compressive loads can be obtained (Fig. 13). For each hydrostatic pressure, the K_{II}^* linearly increases as the axial compressive load and the slopes of the fitting curves for each hydrostatic pressure are identical. Meanwhile, the K_{II}^* for the SCC specimen without hydrostatic pressure can be written as

$$K_{II}^* = \left\{ \left[Y(C/H_l)\sqrt{\pi H_a} \right] / DC \right\} \cdot \pi (D/2)^2 \sigma = \alpha\sigma \tag{10}$$

where σ is the axial loading (MPa) on the ends of the SCC specimen. Thus, the value of α is the slope of the curve without the hydrostatic pressure. Moreover, because the slopes of the curves for each hydrostatic pressure in Fig. 13 are the same, the K_{II}^* of the SCC specimen with the hydrostatic pressure can be expressed as

$$K_{II}^* = \alpha\sigma + \beta\sigma_h \tag{11}$$

Further, to determine the value of β, the values of K_{II}^* are replotted in terms of the hydrostatic pressure in Fig. 14. It can be seen that the K_{II}^* keeps constant as the increase of the hydrostatic pressure and the slopes of the curves for a certain axial compressive load are zero. Hence, the value of β for each hydrostatic pressure is the slope of the arbitrary fitting curve in Fig. 14. Consequently, the values of α and β are determined as α = 0.27 $m^{1/2}$ and β = 0 $m^{1/2}$ for the SCC specimen under hydrostatic pressures in this

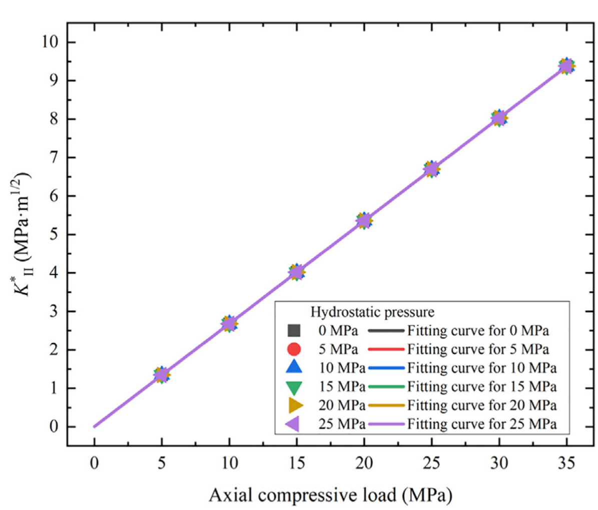

Fig. 13. K_{II}^* in terms of various axial compressive loads.

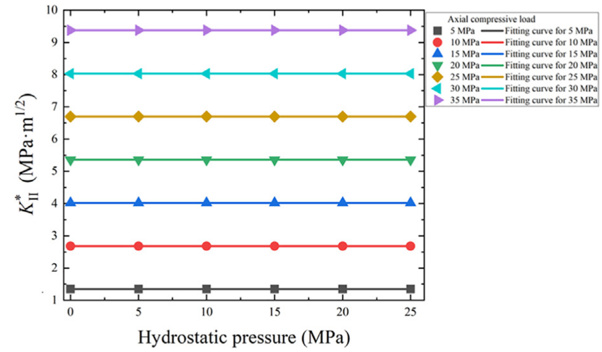

Fig. 14. K_{II}^* in terms of various hydrostatic pressures.

study. In addition, the formula to determine the K_{IIC} of rocks through the SCC specimen under hydrostatic pressures can be rewritten as

$$K_{IIC} = \alpha\sigma_{max} + \beta\sigma_h = 0.27\sigma_{max} + 0 \times \sigma_h = 0.27\sigma_{max} \tag{12}$$

It implies that the rock K_{IIC} is barely affected by the hydrostatic pressure. Based on Eq. (12), the K_{IIC} of rocks under various hydrostatic pressures can be calculated when the geometry of the SCC specimen proposed in this study is used in the dynamic tests.

3.5. Determination of loading rate for the SCC specimen under hydrostatic pressure

With the dynamic stress equilibrium for SCC samples, the time evolution of the dynamic K_{II}^* is deduced from Eq. (11).

$$K_{II}^*(t) = \alpha\sigma(t) + \beta\sigma_h \tag{13}$$

where $\sigma(t)$ is the dynamic compressive stress (MPa). Since the hydrostatic pressure is consistent during the dynamic shear process, the values of α and β in Eq. (12) are also applicable to Eq. (13). Based on the definition of the dynamic loading rate suggested by the ISRM [40], the slope (i.e. the dashed-dot line in Fig. 15) of the almost linear rising section in the SIF-time curve is the loading rate for the dynamic SCC test.

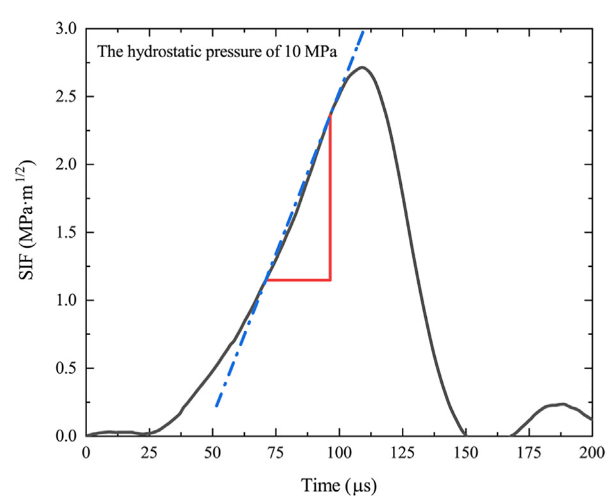

Fig. 15. Dynamic loading rate determination in a typical dynamic SCC test. The loading rate is 48 GPa·$m^{1/2}$/s and K_{IIC} = 2.71 MPa·$m^{1/2}$ in this typical dynamic SCC test.

4. Results and discussions

The SCC specimen failed after a typical dynamic test is shown in Fig. 2b and c. The specimen was sheared separately along the potential fracture plane between these two notch-tips. The failure pattern is consistent with the stress distribution observed in the above numerical analysis and the failure mode reported by other researchers [33,53]. Based on both experimental observation and numerical analysis, the failure mode is Mode Ⅱ and the dynamic SCC specimen is valid to measure the K_{IIC} of rocks.

The dynamic K_{IIC} of FM over different hydrostatic pressures (i.e. 0, 5, 10, 15, and 20 MPa) is shown in Fig. 16. The largest value of dynamic K_{IIC} (4.76 MPa·m$^{1/2}$) was obtained when the hydrostatic pressure is 20 MPa. It indicates that the dynamic K_{IIC} over a given hydrostatic pressure rises as the loading rate. This reveals that the dynamic K_{IIC} of FM has a strong rate dependence, which has been widely found in other mechanical behaviors of rocks (e.g. compressive/tensile strength, Mode I fracture toughness) in literature [76–80]. The K_{IIC} of FM measured through the PTS specimen in the authors' early study [5] is given in Fig. 16. The dynamic K_{IIC} measured by both the SCC specimen and the PTS specimen has a consistent trend in terms of the loading rate. Namely, the dynamic K_{IIC} almost linearly increases with the loading rate for both the SCC specimen and the PTS specimen, and the slope of the linear fitting line based on the dynamic K_{IIC} data points from the SCC specimen is nearly the same as that of the fitting line based on the dynamic K_{IIC} data points from the PTS specimen. The dynamic K_{IIC} of FM under a specific loading rate without hydrostatic pressure in this study has a slight discrepancy with that of FM under the corresponding loading rate by using the PTS specimen. For example, at the loading rate of around 30 GPa·m$^{1/2}$/s, the dynamic K_{IIC} from the SCC specimen is 0.19 MPa·m$^{1/2}$ higher than that from the PTS specimen. This little difference between the values of K_{IIC} derived from these two testing methods is acceptable and may be caused by the diversity of the FM. In addition, at a given loading rate the dynamic rock K_{IIC} is barely affected by the hydrostatic pressure. This is probably attributed to the constant shear stress field around the crack-tips under various hydrostatic pressures. Moreover, Fig. 16 shows the dynamic K_{IC} of FM in the references [58,59]. One can see that the dynamic K_{IIC} under various hydrostatic pressures are bigger than the dynamic K_{IC} over a similar loading rate. This phenomenon was discovered in other types of rocks as well [47].

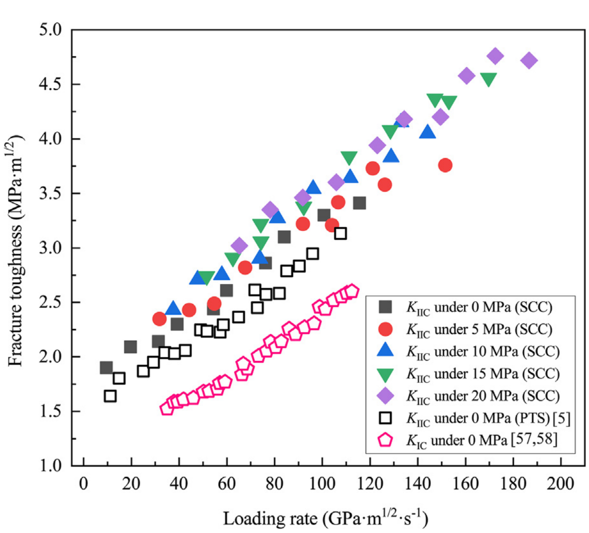

Fig. 16. Fracture toughnesses of FM with different hydrostatic pressures.

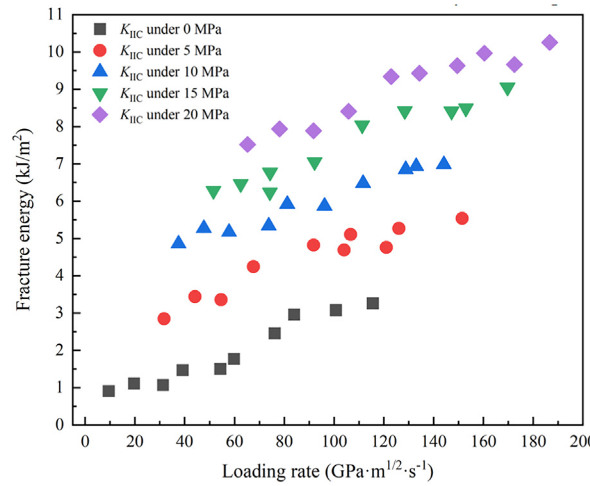

Fig. 17. Dynamic fracture energy of the FM SCC specimen with various hydrostatic pressures.

Fig. 17 gives the dynamic fracture energy of FM over various hydrostatic pressures. At a given hydrostatic pressure, the fracture energy of FM demonstrates a loading rate dependence. This phenomenon is consistent with the observation in the authors' early study by using the dynamic PTS method [5]. Another finding is that the fracture energy of FM under a certain loading rate increases with the hydrostatic pressure. This reveals that the hydrostatic pressure has an apparent effect on the fracture energy in the dynamic SCC tests; that is, during the dynamic shear failure process in the SCC test under a certain loading rate, the more the hydrostatic pressure, the more energy consumed by the creation of the new shear fracture surface.

5. Conclusions

(1) The dynamic rock K_{IIC} over different hydrostatic pressures was studied via a dynamic SCC method. The dynamic SCC specimen was designed following the requirement of the valid dynamic rock test. The hydrostatic pressure was applied to the SCC specimen by two hydraulic cylinders in the dynamic loading system. Pulse shaper was utilized to facilitate the dynamic stress equilibrium in SCC specimens.

(2) The FM was employed in dynamic SCC experiments with hydrostatic pressures. The rock sample was sheared separately along the potential fracture plane between these two notch-tips. The SIF of the dynamic SCC sample was determined by using the FEA with the secondary cracks. The equation for calculating the K_{IIC} of the SCC sample was obtained from the FEA, and the dynamic K_{IIC} of FM can be obtained from the peak dynamic stress and the hydrostatic pressure.

(3) The results of SCC tests indicate that the dynamic K_{IIC} of FM under a certain hydrostatic pressure increases as the loading rate. In addition, at a given loading rate the dynamic rock K_{IIC} is barely affected by the hydrostatic pressure. This is probably attributed to the constant shear stress field around the crack-tips under various hydrostatic pressures.

(4) The K_{IIC} of FM under different hydrostatic pressures is consistently higher than the K_{IC} of FM under the corresponding loading rate. Furthermore, at a given hydrostatic pressure, the fracture energy of FM demonstrates a loading rate dependence.

(5) Another important finding is that the fracture energy of FM under a certain loading rate increases as hydrostatic pressures. This reveals that the hydrostatic pressure has an apparent effect on the fracture energy of rocks in dynamic SCC tests.

Acknowledgements

This research was supported by the Natural Sciences and Engineering Research Council of Canada (NSERC) (No. 72031326) and the National Natural Science Foundation of China (No. 52079091). This study was supported by Academy of Finland under Grant No. 322518. This paper is supported by the opening project of State Key Laboratory of Explosion Science and Technology (Beijing Institute of Technology). The opening project number is KFJJ20-01M.

References

[1] Kim BH, Larson MK. Laboratory investigation of the anisotropic confinement-dependent brittle-ductile transition of a Utah coal. Int J Min Sci Technol 2021;31(1):51–7.
[2] Li DY, Xiao P, Han ZY, Zhu QQ. Mechanical and failure properties of rocks with a cavity under coupled static and dynamic loads. Eng Fract Mech 2020;225:106195.
[3] Lukić B, Forquin P. Experimental characterization of the punch through shear strength of an ultra-high performance concrete. Int J Impact Eng 2016;91:34–45.
[4] Yao W, Xia K, Zhang T. Dynamic fracture test of laurentian granite subjected to hydrostatic pressure. Exp Mech 2019;59(2):245–50.
[5] Yao W, Xu Y, Yu CY, Xia KW. A dynamic punch-through shear method for determining dynamic Mode II fracture toughness of rocks. Eng Fract Mech 2017;176:161–77.
[6] Tian J, Xu D, Liu T. An experimental investigation of the fracturing behaviour of rock-like materials containing two V-shaped parallelogram flaws. Int J Min Sci Technol 2020;30(6):777–83.
[7] Xiao P, Li DY, Zhao GY, Zhu QQ, Liu HX, Zhang CS. Mechanical properties and failure behavior of rock with different flaw inclinations under coupled static and dynamic loads. J Central South Univ 2020;27(10):2945–58.
[8] Hao X, Du W, Zhao Y, Sun Z, Zhang Q, Wang S, Qiao H. Dynamic tensile behaviour and crack propagation of coal under coupled static-dynamic loading. Int J Min Sci Technol 2020;30(5):659–68.
[9] Chen F, Cao P, Rao QH, Ma CD, Sun ZQ. A mode II fracture analysis of double edge cracked Brazilian disk using the weight function method. Int J Rock Mech Min Sci 2005;42(3):461–5.
[10] Wei MD, Dai F, Xu NW, Zhao T. Stress intensity factors and fracture process zones of ISRM-suggested chevron notched specimens for mode I fracture toughness testing of rocks. Eng Fract Mech 2016;168:174–89.
[11] Li DY, Gao FH, Han ZY, Zhu QQ. Full- and local-field strain evolution and fracture behavior of precracked granite under coupled static and dynamic loads. Shock Vib 2020;2020:1–15.
[12] Li DY, Gao FH, Han ZY, Zhu QQ. Experimental evaluation on rock failure mechanism with combined flaws in a connected geometry under coupled static-dynamic loads. Soil Dyn Earthq Eng 2020;132:106088.
[13] Anderson TL, Anderson TL. Fracture mechanics: fundamentals and applications. CRC Press; 2005.
[14] Aliha MRM, Ayatollahi MR. Rock fracture toughness study using cracked chevron notched Brazilian disc specimen under pure modes I and II loading - A statistical approach. Theor Appl Fract Mech 2014;69:17–25.
[15] Fowell RJ. Suggested method for determining mode I fracture toughness using Cracked Chevron Notched Brazilian Disc (CCNBD) specimens. Int J Rock Mech Min Sci Geomech Abstr 1995;32(1):57–64.
[16] Iqbal MJ, Mohanty B. Experimental calibration of ISRM suggested fracture toughness measurement techniques in selected brittle rocks. Rock Mech Rock Eng 2006;40(5):453–75.
[17] Dai F, Wei MD, Xu NW, Ma Y, Yang DS. Numerical assessment of the progressive rock fracture mechanism of cracked chevron notched Brazilian disc specimens. Rock Mech Rock Eng 2015;48(2):463–79.
[18] Franklin J, Sun Z, Atkinson B, Meredith P, Rummel F, Mueller W, Nishimatsu Y, Takahahsi H, Costin LS, Ingraffea AR, Bobrov GF. Suggested methods for determining the fracture toughness of rock. Int J Rock Mech Min Sci Geomech Abstr 1988;25(2):71–96.
[19] Mostafavi M, McDonald SA, Mummery PM, Marrow TJ. Observation and quantification of three-dimensional crack propagation in poly-granular graphite. Eng Fract Mech 2013;110:410–20.
[20] Zhang ZX, Kou SQ, Yu J, Yu Y, Jiang LG, Lindqvist PA. Effects of loading rate on rock fracture. Int J Rock Mech Min Sci 1999;36(5):597–611.
[21] Kuruppu MD, Obara Y, Ayatollahi MR, Chong KP, Funatsu T. ISRM-suggested method for determining the mode I static fracture toughness using semi-circular bend specimen. Rock Mech Rock Eng 2014;47(1):267–74.
[22] Aliha MRM, Ayatollahi MR. Brittle fracture evaluation of a fine grain cement mortar in combined tensile-shear deformation. Fatigue Fract Eng Mater Struct 2009;32(12):987–94.
[23] Fakhri M, Amoosoltani E, Aliha MRM. Crack behavior analysis of roller compacted concrete mixtures containing reclaimed asphalt pavement and crumb rubber. Eng Fract Mech 2017;180:43–59.
[24] Ingraffea AR. Mixed-Mode Fracture Initiation In Indiana Limestone And Westerly Granite. In: Proceedings of the 22nd US Symposium on Rock Mechanics (USRMS). Cambridge, Massachusetts: American Rock Mechanics Association; 1981.
[25] Razavi SMJ, Aliha MRM, Berto F. Application of an average strain energy density criterion to obtain the mixed mode fracture load of granite rock tested with the cracked asymmetric four-point bend specimens. Theor Appl Fract Mech 2018;97:419–25.
[26] Swartz SE, Lu LW, Tang LD, Refai TME. Mode II fracture-parameter estimates for concrete from beam specimens. Exp Mech 1988;28(2):146–53.
[27] Li M, Sakai M. Mixed-mode fracture of ceramics in asymmetric four-point bending: effect of crack-face grain interlocking/bridging. J Am Ceram Soc 1996;79(10):2718–26.
[28] Shi YW, Zhou NN. Comparison of microshear toughness and mode II fracture toughness for structural steels. Eng Fract Mech 1995;51(4):669–77.
[29] Ayatollahi MR, Aliha MRM. On the use of an anti-symmetric four-point bend specimen for mode II fracture experiments. Fatigue Fract Eng Mater Struct 2011;34(11):898–907.
[30] Backers T, Dresen G, Rybacki E, Stephansson O. New data on mode II fracture toughness of rock from the punchthrough shear test. Int J Rock Mech Min Sci 2004;41:2–7.
[31] Backers T, Stephansson O, Rybacki E. Rock fracture toughness testing in Mode II—punch-through shear test. Int J Rock Mech Min Sci 2002;39(6):755–69.
[32] Davies J, Morgan TG, Yim AW. The finite element analysis of a punch-through shear specimen in mode II. Int J Fract 1985;28(1):R3–R10.
[33] Xu Y, Yao W, Zhao GL, Xia KW. Evaluation of the short core in compression (SCC) method for measuring mode II fracture toughness of rocks. Eng Fract Mech 2020;224:106747.
[34] Arcan M, Hashin Z, Voloshin A. A method to produce uniform plane-stress states with applications to fiber-reinforced materials. Exp Mech 1978;18(4):141–6.
[35] Hasanpour R, Choupani N. Rock fracture characterization using the modified Arcan test specimen. Int J Rock Mech Min Sci 2009;46(2):346–54.
[36] Fathipour Azar H, Choupani N, Afshin H, Hamidzadeh MR. Effect of mineral admixtures on the mixed-mode (I/II) fracture characterization of cement mortar: CTS, CSTBD and SCB specimens. Eng Fract Mech 2015;134:20–34.
[37] Xie YS, Cao P, Jin J, Wang M. Mixed mode fracture analysis of semi-circular bend (SCB) specimen: A numerical study based on extended finite element method. Comput Geotech 2017;82:157–72.
[38] Ayatollahi MR, Aliha MRM, Hassani MM. Mixed mode brittle fracture in PMMA—An experimental study using SCB specimens. Mater Sci Eng: A 2006;417(1–2):348–56.
[39] Chang SH, Lee CI, Jeon S. Measurement of rock fracture toughness under modes I and II and mixed-mode conditions by using disc-type specimens. Eng Geol 2002;66(1–2):79–97.
[40] Zhou YX, Xia K, Li XB, Li HB, Ma GW, Zhao J, Zhou ZL, Dai F. Suggested methods for determining the dynamic strength parameters and mode-I fracture toughness of rock materials. Int J Rock Mech Min Sci 2012;49:105–12.
[41] Atkinson BK. Fracture toughness of Tennessee Sandstone and Carrara Marble using the double torsion testing method. Int J Rock Mech Min Sci Geomech Abstr 1979;16(1):49–53.
[42] Ayatollahi MR, Aliha MRM. Cracked Brazilian disc specimen subjected to mode II deformation. Eng Fract Mech 2005;72(4):493–503.
[43] Rao QH, Sun ZQ, Stephansson O, Li CL, Stillborg B. Shear fracture (Mode II) of brittle rock. Int J Rock Mech Min Sci 2003;40(3):355–75.
[44] Wei MD, Dai F, Xu NW, Liu Y, Zhao T. Fracture prediction of rocks under mode I and mode II loading using the generalized maximum tangential strain criterion. Eng Fract Mech 2017;186:21–38.
[45] Xu NW, Dai F, Wei MD, Xu Y, Zhao T. Numerical Observation of Three-Dimensional Wing Cracking of Cracked Chevron Notched Brazilian Disc Rock Specimen Subjected to Mixed Mode Loading. Rock Mech Rock Eng 2016;49(1):79–96.
[46] Watkins J, Liu KLW. A finite element study of the short beam test specimen under mode II loading. Int J Cem Compos Light Concr 1985;7(1):39–47.
[47] Backers T, Stephansson O. ISRM Suggested Method for the Determination of Mode II Fracture Toughness. Rock Mech Rock Eng 2012;45(6):1011–22.
[48] Hakami H, Stephansson O. Shear fracture energy of Stripa granite- results of controlled triaxial testing. Eng Fract Mech 1990;35(4–5):855–65.
[49] Lawn B. Fracture of brittle solids. Cambridge: Cambridge University Press; 1993.
[50] Melin S. When does a crack grow under mode II conditions? Int J Fract 1986;30(2):103–14.
[51] Whittaker B, Singh R, Sun G. Rock Fracture Mechanics - Principles, Design and Applications. Amsterdam: Elsevier Science Publisher; 1992.
[52] Lee JS. Time-dependent crack growth in brittle rocks and field applications to geologic hazards. Michigan: ProQuest; 2007.
[53] Jung Y, Park E, Kim H. Determination of mode II toughness of granite by using SCC test. In: Proceedings of the ISRM International Symposium - EUROCK 2016. Ürgüp; 2016.

[54] Jung Y, Park E, Kim H. Determination of mode II toughness of granite by using SCC test. In: Proceedings of the ISRM International Symposium - EUROCK 2016. Ürgüp; 2016.
[55] Yao W, Xu Y, Xia KW, Wang S. Dynamic mode II fracture toughness of rocks subjected to confining pressure. Rock Mech Rock Eng 2020;53(2):569–86.
[56] Xia KW, Yao W. Dynamic rock tests using split Hopkinson (Kolsky) bar system - A review. J Rock Mech Geotech Eng 2015;7(1):27–59.
[57] Yao W, He TM, Xia KW. Dynamic mechanical behaviors of Fangshan marble. J Rock Mech Geotech Eng 2017;9(5):807–17.
[58] Zhang QB, Zhao J. Effect of loading rate on fracture toughness and failure micromechanisms in marble. Eng Fract Mech 2013;102:288–309.
[59] Zhang QB, Zhao J. Determination of mechanical properties and full-field strain measurements of rock material under dynamic loads. Int J Rock Mech Min Sci 2013;60:423–39.
[60] Wu BB, Yao W, Xia KW. An experimental study of dynamic tensile failure of rocks subjected to hydrostatic confinement. Rock Mech Rock Eng 2016;49(10):3855–64.
[61] Wu BB, Chen R, Xia KW. Dynamic tensile failure of rocks under static pre-tension. Int J Rock Mech Min Sci 2015;80:12–8.
[62] Chen WW, Song B. Split Hopkinson (Kolsky) Bar: Design, Testing and Applications. New York: Springer; 2010.
[63] Song B, Chen W. Energy for specimen deformation in a split Hopkinson pressure bar experiment. Exp Mech 2006;46(3):407–10.
[64] Chen R, Xia K, Dai F, Lu F, Luo SN. Determination of dynamic fracture parameters using a semi-circular bend technique in split Hopkinson pressure bar testing. Eng Fract Mech 2009;76(9):1268–76.
[65] Rice JR. A path independent integral and the approximate analysis of strain concentration by notches and cracks. J Appl Mech 1968;35(2):379–86.
[66] Cherepanov GP. Crack propagation in a continuum. Prikl Mat Mekh 1967;31(3):476–88.
[67] Lim IL, Johnston IW, Choi SK. Stress intensity factors for semi-circular specimens under three-point bending. Eng Fract Mech 1993;44(3):363–82.
[68] Simulia D. Abaqus 6.11 analysis user's manual. 2011.
[69] Horii H, Nemat-Nasser S. Brittle failure in compression: splitting faulting and brittle-ductile transition. Phil Trans R Soc Lond A 1986;319(1549):337–74.
[70] Horii H, Nemat-Nasser S. Compression-induced microcrack growth in brittle solids: Axial splitting and shear failure. J Geophys Res: Solid Earth 1985;90(B4):3105–25.
[71] Nemat-Nasser S, Horii H. Compression-induced nonplanar crack extension with application to splitting, exfoliation, and rockburst. J Geophys Res: Solid Earth 1982;87(B8):6805–21.
[72] Atkinson BK. Introduction to fracture mechanics and its geophysical applications. In: Fracture Mechanics of Rock. Amsterdam: Elsevier; 1987. p. 1–26.
[73] Ayatollahi MR, Mahdavi E, Alborzi MJ, Obara Y. Stress intensity factors of semi-circular bend specimens with straight-through and chevron notches. Rock Mech Rock Eng 2016;49(4):1161–72.
[74] Aliha MRM, Pakzad R, Ayatollahi MR. Numerical analyses of a cracked straight-through flattened Brazilian disk specimen under mixed-mode loading. J Eng Mech 2014;140(1):219–24.
[75] Chan SK, Tuba IS, Wilson WK. On the finite element method in linear fracture mechanics. Eng Fract Mech 1970;2(1):1–17.
[76] Dai F, Xia K, Luo SN. Semicircular bend testing with split Hopkinson pressure bar for measuring dynamic tensile strength of brittle solids. Rev Sci Instrum 2008;79(12):123903.
[77] Dai F, Xia KW, Tang LZ. Rate dependence of the flexural tensile strength of Laurentian granite. Int J Rock Mech Min Sci 2010;47(3):469–75.
[78] Huang S, Chen R, Xia KW. Quantification of dynamic tensile parameters of rocks using a modified Kolsky tension bar apparatus. J Rock Mech Geotech Eng 2010;2(2):162–8.
[79] Huang S, Xia KW. Effect of heat-treatment on the dynamic compressive strength of Longyou sandstone. Eng Geol 2015;191:1–7.
[80] Feng JJ, Wang EY, Huang QS, Ding HC, Zhang XY. Experimental and numerical study of failure behavior and mechanism of coal under dynamic compressive loads. Int J Min Sci Technol 2020;30(5):613–21.